

Phosphoregulation of Tau modulates inhibition of kinesin-1 motility

Jamie L. Stern^{a,b}, Dominique V. Lessard^{a,b}, Gregory J. Hoepflich^b, Gerardo A. Morfini^c, and Christopher L. Berger^{a,b,*}

^aCellular, Molecular and Biomedical Sciences Program and ^bDepartment of Molecular Physiology and Biophysics, University of Vermont, Burlington, VT 05405; ^cDepartment of Anatomy and Cell Biology, University of Illinois at Chicago, Chicago, IL 60612

ABSTRACT Microtubule-based axonal transport is tightly regulated by numerous pathways, ensuring appropriate delivery of specific organelle cargoes to selected subcellular domains. Highlighting the importance of this process, pathological evidence has linked alterations in these pathways to the pathogenesis of several neurodegenerative diseases. An important regulator of this system, the microtubule-associated protein Tau, has been shown to participate in signaling cascades, modulate microtubule dynamics, and preferentially inhibit kinesin-1 motility. However, the cellular means of regulating Tau's inhibition of kinesin-1 motility remains unknown. Tau is subject to various posttranslational modifications, including phosphorylation, but whether phosphorylation regulates Tau on the microtubule surface has not been addressed. It has been shown that tyrosine 18 phosphorylated Tau regulates inhibition of axonal transport in the disease state. Tyrosine 18 is both a disease- and nondisease-state modification and is therefore an attractive starting point for understanding control of Tau's inhibition of kinesin-1 motility. We show that pseudophosphorylation of tyrosine 18 reduces 3RS-Tau's inhibition of kinesin-1 motility. In addition, we show that introduction of negative charge at tyrosine 18 shifts Tau's previously described static–dynamic state binding equilibrium toward the dynamic state. We also present the first evidence of Tau's static–dynamic state equilibrium under physiological conditions.

Monitoring Editor

David G. Drubin
University of California,
Berkeley

Received: Oct 24, 2016

Revised: Jan 30, 2017

Accepted: Feb 22, 2017

INTRODUCTION

The neuronal microtubule-associated protein (MAP) Tau is involved in axonal development from its earliest stages onward (Andreadis, 2005). Tau has been implicated in many processes within the neu-

ron, the majority of which are associated with its participation in axonal transport (AT). The AT system encompasses the microtubule track, molecular motors, including kinesin-1 and -2, numerous MAPs, including Tau, and many signaling cascades (Maday *et al.*, 2014). Tau's role in AT is multifaceted; it has been shown to stabilize microtubules (Panda *et al.*, 2003), participate in signaling cascades (Kanaan *et al.*, 2012), and inhibit kinesin-1 motility (Vershinin *et al.*, 2007; Dixit *et al.*, 2008; McVicker *et al.*, 2011). In the nondisease state, Tau's ability to preferentially inhibit kinesin-1 motility is of particular interest when juxtaposed with the failure of this inhibition to disrupt normal cargo delivery, suggesting that Tau has a role in the modulation of kinesin-mediated cargo delivery during AT (Kanaan *et al.*, 2012). This highlights the importance of cellular regulation of Tau's inhibition of kinesin-1 transport during AT, but how this control is achieved is unknown.

Understanding Tau's function and corresponding regulation is compounded by its sequence diversity. There are six Tau isoforms, which arise from strict developmental regulation of the alternative splicing of the *MAPT* gene on chromosome 17 (Andreadis, 2005;

This article was published online ahead of print in MBoc in Press (<http://www.molbiolcell.org/cgi/doi/10.1091/mbc.E16-10-0728>) on March 1, 2017.

The authors declare no conflicts of interest with regard to the work presented here.

The manuscript was written by J.S. and C.B. J.S., C.B., and G.M. participated in editing. Experiments were designed by J.S., G.H., G.M., and C.B. and performed by J.S., D.L., and G.H.

*Address correspondence to: Christopher L. Berger (cberger@uvm.edu).

Abbreviations used: AT, axonal transport; BRB80, Brinkley's Reassembly Buffer 80; BRB80+OS, BRB80 and oxygen scavengers; MAP, microtubule-associated protein; PAD, phosphatase-activating domain; PP1, protein phosphatase 1; Y18, tyrosine 18.

© 2017 Stern *et al.* This article is distributed by The American Society for Cell Biology under license from the author(s). Two months after publication it is available to the public under an Attribution–Noncommercial–Share Alike 3.0 Unported Creative Commons License (<http://creativecommons.org/licenses/by-nc-sa/3.0>).

"ASCB®," "The American Society for Cell Biology®," and "Molecular Biology of the Cell®" are registered trademarks of The American Society for Cell Biology.

Ballatore *et al.*, 2007). Whereas all six isoforms have a central proline-rich region (PRR) and N-terminal phosphatase-activating domain (PAD; Ballatore *et al.*, 2007; Kanaan *et al.*, 2012), they differ in the number of C-terminal microtubule-binding repeats (three or four) and N-terminal acidic inserts (zero to two; Goode *et al.*, 2000; Ballatore *et al.*, 2007). Tau's role in signaling is partly mediated by its PAD, which activates protein phosphatase 1 (PP1; LaPointe *et al.*, 2009; Kanaan *et al.*, 2011). In the disease state, a phosphomimetic of tyrosine 18 (Y18), the last residue in the PAD, prevents inhibition of axonal transport when incorporated into neurofibrillary tangles (Kanaan *et al.*, 2012). Y18 is predominantly phosphorylated by the Src family kinase Fyn in both the disease and nondisease states (Lee *et al.*, 1998; Kanaan *et al.*, 2012; Larson *et al.*, 2012).

Adding to this isoform diversity, it been shown that Tau can bind the microtubule in an equilibrium between static and ATP-independent dynamic states (Vershinin *et al.*, 2007; Dixit *et al.*, 2008; Hinrichs *et al.*, 2012). We showed that the static–dynamic state equilibrium differs with Tau isoform and microtubule lattice structure, with the shortest isoform, 3RS-Tau, being more static on paclitaxel stabilized microtubules than the longest isoform, 4RL-Tau (McVicker *et al.*, 2014). Tau's ability to inhibit kinesin-1 motility also differs with isoform. 3RS-Tau, which favors the static state, is more inhibitory to kinesin-1 than 4RL-Tau (Dixit *et al.*, 2008; McVicker *et al.*, 2011). This correlation indicates that the static state is more inhibitory to kinesin-1 motility than the dynamic state. Given these isoform-specific differences in behavior, a common mechanism for regulating multiple Tau isoforms and their static–dynamic state equilibria remains unclear.

All isoforms of Tau are subject to a variety of post-translational modifications (PTMs; Watanabe *et al.*, 1993; Funk *et al.*, 2014; Kamah *et al.*, 2014), which may have important roles in many aspects of Tau regulation. We postulate that PTMs (especially phosphorylation) are the link between controlling Tau's static–dynamic equilibrium and Tau's inhibition of kinesin-1 motility. As stated earlier, static Tau is more inhibitory to kinesin-1 motility than dynamic Tau (McVicker *et al.*, 2011), whereas phosphorylation/a phosphomimetic of Y18 has been shown to prevent inhibition of axonal transport in the disease state (Kanaan *et al.*, 2012). We hypothesize that the negative charge provided by phosphorylation of Y18 stabilizes the dynamic state/destabilizes the static state, thereby shifting the static–dynamic equilibrium toward the less inhibitory dynamic state. To test this hypothesis, we generated phosphomimetic and control 3RS-Tau constructs by mutating Y18 to glutamic acid (Y18E 3RS-Tau) and alanine (Y18A 3RS-Tau). To study the effect of increasing the negative charge at/around Y18, we generated a double phosphomimetic by mutating threonine 17 and Y18 to glutamic acid (dE 3RS-Tau). Using total internal reflection fluorescence (TIRF) microscopy, we observed single-molecule 3RS-Tau interactions with paclitaxel-stabilized microtubules. Our results provide the first evidence for direct control by phosphorylation of Tau's dynamic behavior, and therefore its function, on the microtubule surface.

RESULTS

Introduction of negative charge at Y18 reduces 3RS-Tau inhibition of kinesin-1 motility

TIRF microscopy was used to visualize kinesin-1 motility (Figure 1 and Supplemental Movies S1 and S2) on paclitaxel-stabilized microtubules in the presence of 200 nM unlabeled and Alexa 488-labeled wild-type (WT) and Y18E 3RS-Tau (1:5 Tau:tubulin; Figure 2A). In the absence of Tau, kinesin-1 had a run length of $1.64 \pm 0.50 \mu\text{m}$ (Figure 2B), which significantly decreased in the presence of both unlabeled and labeled WT 3RS-Tau (0.99 ± 0.23 and $0.99 \pm 0.24 \mu\text{m}$; Figure 2, C and D, Supplemental Table S2, and Supplemental

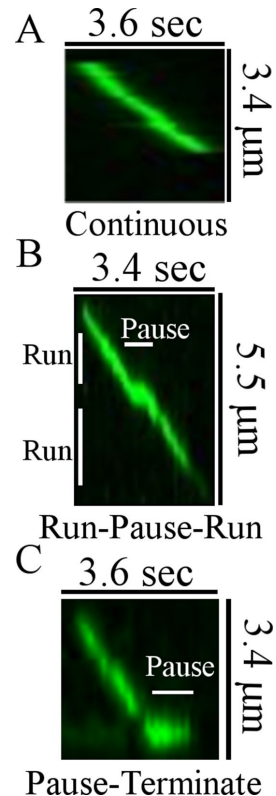


FIGURE 1: Representative kymographs of kinesin-1 motility. TIRF microscopy was used to observe kinesin-1 motility in the absence of Tau and in the presence of unlabeled or Alexa 488-labeled WT and Y18E 3RS-Tau (200 nM [1:5 Tau:tubulin]). (A) Continuous, (B) run-pause-run, and (C) pause-terminate events were observed under all conditions.

Figure S1), as we previously demonstrated (McVicker *et al.*, 2011). Of interest, however, kinesin-1's run length significantly increased in the presence of Y18E 3RS-Tau (unlabeled, $1.37 \pm 0.39 \mu\text{m}$; labeled, $1.35 \pm 0.39 \mu\text{m}$; Figure 2, E and F, and Supplemental Movie S1) compared with the WT 3RS-Tau condition (Figure 2, C and D, and Supplemental Movie S2). Kinesin-1's velocity did not differ under any of the conditions tested (Supplemental Table S2). These results indicate that introduction of negative charge at Y18 reduces 3RS-Tau's inhibition of kinesin-1 run length without affecting its velocity. WT Tau's ability to inhibit kinesin-1 run length without affecting velocity was reported previously (Dixit *et al.*, 2008). This is the first evidence for phosphorylation-mediated regulation of 3RS-Tau's ability to inhibit kinesin-1 motility.

A Y18 phosphomimetic of 3RS-Tau exhibits a significant shift toward the dynamic state in vitro

Given the results of our motility assays, we wanted to know whether the introduction of negative charge at Y18 affects Tau's static–dynamic equilibrium on the microtubule surface. TIRF microscopy was used to visualize the interactions of Tau used in the motility assays (WT and Y18E 3RS-Tau; Figure 3A), with tetramethylrhodamine isothiocyanate rhodamine-labeled, paclitaxel-stabilized microtubules at 200 nM Tau (1:5 Tau:tubulin). We observed predominantly static events for WT 3RS-Tau ($77.1 \pm 4.2\%$; Figure 3B, Supplemental Table S3, and Supplemental Movie S3), a result we previously demonstrated (McVicker *et al.*, 2014). Conversely, we observed a significant decrease ($p < 0.05$) in the number of static events for Y18E 3RS-Tau ($47.7 \pm 5.0\%$; Figure 3B and Supplemental Table S3).

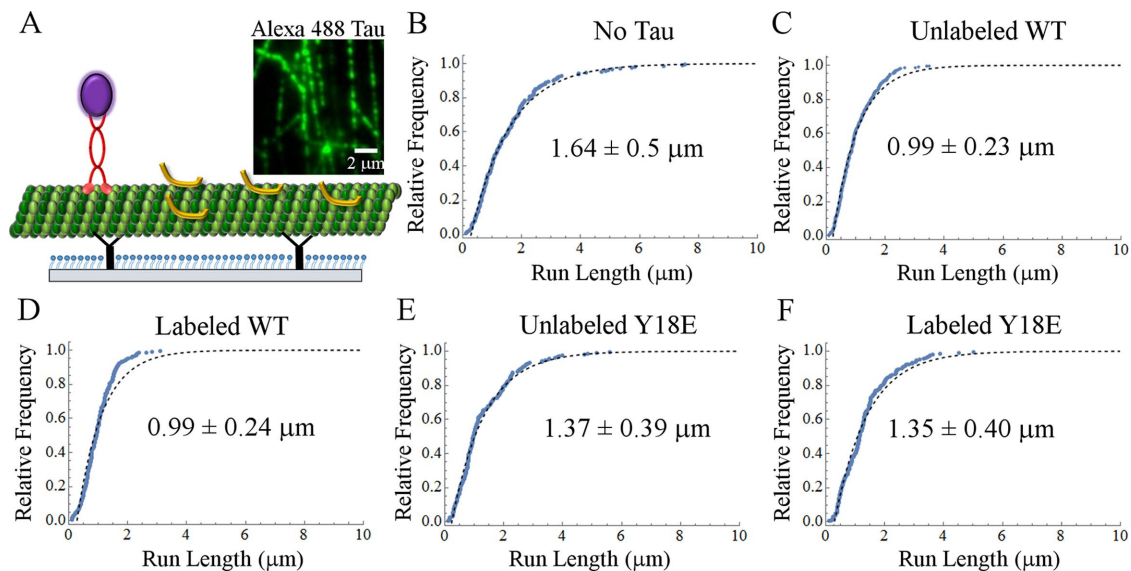


FIGURE 2: Diagram of motility assays with cumulative frequency plots of run lengths (mean \pm SD) for kinesin-1 in the absence and presence of 3RS-Tau. (A) Flow chambers were passivated with PEG-silane (blue) before tubulin antibodies (black) were used to adhere paclitaxel-stabilized microtubules (green). Q-dot-labeled kinesin-1 (purple/red) motility was observed on undecorated or labeled/unlabeled Tau (yellow) decorated microtubules. Inset: unlabeled microtubules coated with 200 nM Alexa 488-labeled Tau. (B) On undecorated microtubules, kinesin-1 had a run length of $1.64 \pm 0.50 \mu\text{m}$. Introduction of both unlabeled (C) and labeled (D) WT 3RS-Tau significantly reduced kinesin-1 run length to 0.99 ± 0.23 and $0.99 \pm 0.24 \mu\text{m}$ ($p < 0.05$). In the presence of unlabeled (E) and labeled (F) Y18E 3RS-Tau, kinesin-1 run length was significantly increased to $1.37 \pm 0.39 \mu\text{m}$ ($p < 0.05$) and $1.35 \pm 0.40 \mu\text{m}$ ($p < 0.05$), respectively. Introduction of negative charge reduced Tau's ability to inhibit kinesin-1 motility and led to a significant increase in run length (Supplemental Table S2). Ten experiments.

Static dwell times for WT 3RS-Tau were best fit to a two-phase exponential function. This revealed one population of long dwell times and one of short dwell times (Supplemental Figures S2A and S3 and Supplemental Table S3), most likely corresponding to the

small, multiprotein complexes (long dwell times) and single-molecule interactions (short dwell times) with the microtubule surface that we previously observed in the static state (McVicker *et al.*, 2014). Y18E 3RS-Tau static dwell times were best fit to a one-phase exponential function (Supplemental Figures S2B and S3 and Supplemental Table S3), with an average of 14.5 s, which is comparable to WT 3RS-Tau's long static dwell time of 15.7 s. Dynamic dwell times for both WT and Y18E 3RS-Tau were best fit to one-phase exponential functions (Supplemental Figure S2, C and D, Supplemental Figure S3, and Supplemental Table S3) and did not differ from each other. The ability to control the equilibrium between the static and dynamic states of Tau and specifically regulate that control by mimicking phosphorylation at Y18 has not been previously demonstrated.

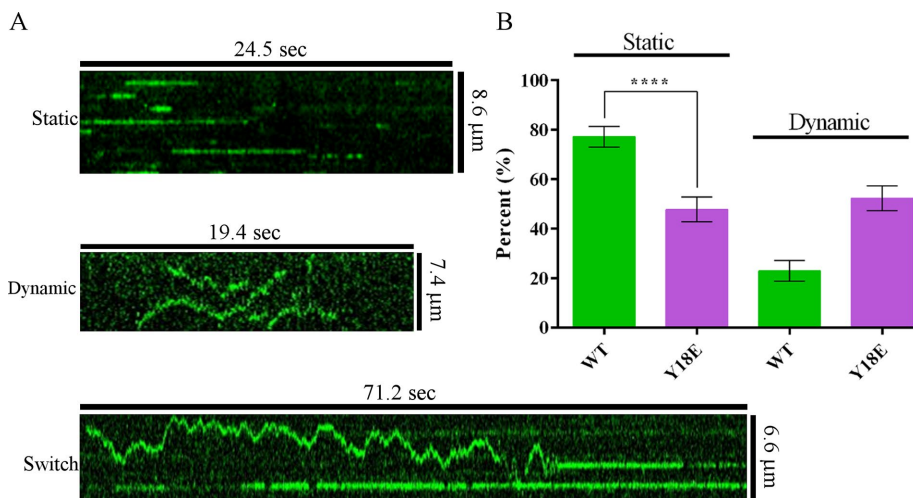


FIGURE 3: Comparison of WT and Y18E 3RS-Tau behavior on Taxol-stabilized microtubules at high concentration. (A) Representative kymographs show the different types of behaviors that can be observed. Tau can bind statically (Static: horizontal lines) while interacting with the microtubule or exhibit dynamic binding along the microtubule surface (Dynamic: jagged lines). Tau can also switch between these states (Switch). (B) Bar graph comparing the percentage (\pm SD) of static to dynamic events for WT and Y18E 3RS-Tau. For WT 3RS-Tau, $77.1 \pm 4.2\%$ of events were static, whereas Y18E 3RS-Tau's equilibrium was shifted toward the dynamic state ($47.7 \pm 5.0\%$ static events). ****Statistically significant difference of $p < 0.05$. Events: WT, 388, and Y18E, 235, from eight experiments.

Y18E 3RS-Tau static dwell times were best fit to a one-phase exponential function (Supplemental Figures S2B and S3 and Supplemental Table S3), with an average of 14.5 s, which is comparable to WT 3RS-Tau's long static dwell time of 15.7 s. Dynamic dwell times for both WT and Y18E 3RS-Tau were best fit to one-phase exponential functions (Supplemental Figure S2, C and D, Supplemental Figure S3, and Supplemental Table S3) and did not differ from each other. The ability to control the equilibrium between the static and dynamic states of Tau and specifically regulate that control by mimicking phosphorylation at Y18 has not been previously demonstrated.

Phosphomimetic constructs of Y18 3RS-Tau bind with decreased affinity for the microtubule

Given the observed shift toward the dynamic state, we considered the possibility that the introduction of negative charge at Y18 reduced Tau's affinity for the microtubule surface. This would also lead to a decrease in 3RS-Tau's ability to inhibit kinesin-1 motility. To address this, we used TIRF microscopy to image increasing concentrations (50–650 nM) of Alexa 532-labeled

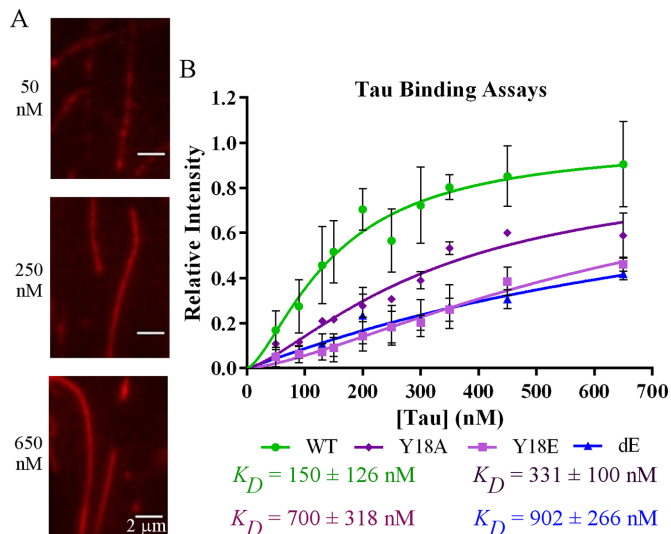


FIGURE 4: Comparison of TIRF binding assays. TIRF binding assays for WT ($N = 4$), Y18A ($N = 3$), Y18E ($N = 3$), and dE ($N = 3$) 3RS-Tau. WT 3RS-Tau had a K_D (mean \pm SD) of 150 ± 126 nM, Y18A 3RS-Tau had $K_D = 331 \pm 100$ nM, Y18E 3RS-Tau had $K_D = 700 \pm 318$ nM, and dE 3RS-Tau had a $K_D = 902 \pm 266$ nM. The affinity of Tau for the microtubule surface decreases with the introduction of increasing negative charge at Y18.

3RS-Tau binding to HiLyte 488-labeled, paclitaxel-stabilized microtubules (Figure 4A). An unphosphorylatable construct (Y18A 3RS-Tau) and a construct with increased negative charge (dE 3RS-Tau) were observed alongside WT and Y18E 3RS-Tau in an effort to better understand the effect of the introduction of negative charge. The average intensity of Alexa 532-labeled 3RS-Tau per unit length along the microtubule was measured and plotted against Tau concentration. The plots were then fitted to one-site-specific binding curves, from which K_D was determined. We found that WT 3RS-Tau binds the microtubule with $K_D = 150 \pm 126$ nM, whereas Y18A 3RS-Tau had $K_D = 331 \pm 100$ nM (Figure 4B and Supplemental Table S3). Introduction of increasing negative charge decreased the affinity of Tau for the microtubule, as evidenced by $K_D = 700 \pm 318$ nM for Y18E 3RS-Tau, with an even greater decrease for dE 3RS-Tau ($K_D = 902 \pm 266$ nM; Figure 4B and Supplemental Table S3).

Phosphomimetic mediated shift toward the dynamic state is maintained for comparable bound fractions of 3RS-Tau

Using the K_D values from our binding assays, we determined that at a microtubule concentration of $1 \mu\text{M}$, WT 3RS-Tau had a bound fraction of 87%, whereas Y18E 3RS-Tau's bound fraction was 59%. At the high concentration used in our kinesin-1 motility assays (200 nM; 1:5 Tau:tubulin), WT 3RS-Tau would have a microtubule-bound concentration of 174 nM, whereas Y18E 3RS-Tau would have 118 nM bound. The inhibition of kinesin-1 by Y18E 3RS-Tau that we observed for this high concentration could then be attributed to this difference in bound fraction of Tau. To address this possibility, we observed WT, control (Y18A), and phosphomimetic (Y18E, dE) constructs of 3RS-Tau at 10 nM (1:3000 Tau:tubulin), where the bound concentrations of WT (9 nM), Y18A (7 nM), Y18E (7 nM), and dE (5 nM) 3RS-Tau were comparable. At this concentration, the percentage of static events for Y18A ($77.8 \pm 4.2\%$) was not significantly different from that for WT 3RS-Tau ($81.4 \pm 3.9\%$; Figure 5 and Supplemental Table S3). Under these conditions, Y18E 3RS-Tau had a static population of $67.4 \pm 4.7\%$ (Figure 5 and Supplemental Table S3),

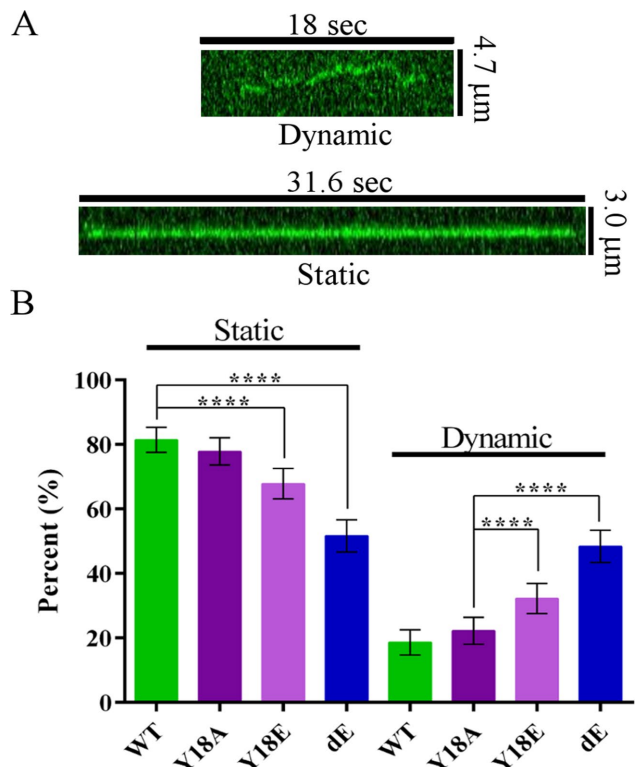


FIGURE 5: Behavior of comparable bound fractions of WT, Y18A, Y18E, and dE 3RS-Tau on paclitaxel-stabilized microtubules. (A) Representative kymographs show both dynamic (jagged line) and static binding along the microtubule surface (horizontal lines). (B) Bar graph comparing the percentage of static to dynamic events (percentage \pm SD) for each Tau construct. Introduction of negative charges at Y18 and T17 shifted the equilibrium between the static and dynamic states toward the dynamic state. ****Statistically significant difference of $p < 0.05$. Events: WT, 566 ($N = 12$); Y18A, 320 ($N = 5$); Y18E, 472 ($N = 4$); and dE, 220 ($N = 5$).

which was a statistically significant difference from WT 3RS-Tau ($p < 0.05$) and Y18A 3RS-Tau ($p < 0.05$; Figure 5 and Supplemental Table S3). dE 3RS-Tau had a static population of $51.4 \pm 5.0\%$ (Figure 5 and Supplemental Table S3), which was a statistically significant decrease compared with Y18E 3RS-Tau ($p < 0.05$).

Dynamic state dwell times for WT, Y18A, Y18E, and dE 3RS-Tau (Supplemental Figure S4, A–D, and Supplemental Table S3) were best fit to one-phase exponential functions and did not significantly differ. Dwell times for static events from WT, Y18A, Y18E, and dE 3RS-Tau populations were best fit to two-phase exponential functions (Supplemental Figure S5, A–D). Although there was a slight decrease in the long and short dwell times for Y18E 3RS-Tau (Supplemental Figure S5C and Supplemental Table S3) and an increase in the short dwell time for dE 3RS-Tau (Supplemental Figure S5D and Supplemental Table S3), the WT, Y18A and dE 3RS-Tau dwell times (long) were not appreciably different. This result indicates that the observed shift toward the dynamic state is independent of the fraction of Tau bound to the microtubule.

Negative charge-mediated shift toward the dynamic state is maintained ex vivo

All the *in vitro* assays presented here were performed at low ionic strength. We therefore asked whether the effect of negative charge on 3RS-Tau's behavior was still present under physiologically relevant

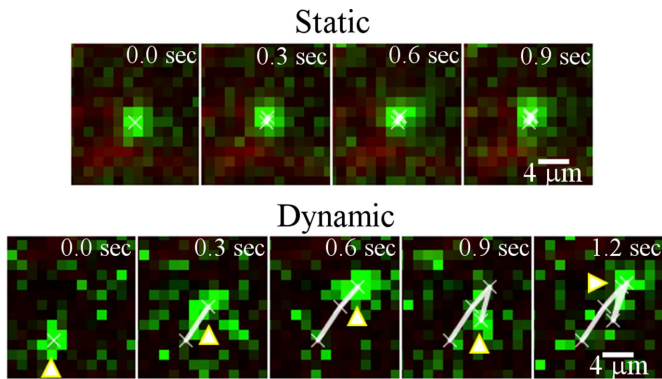


FIGURE 6: Static and dynamic (arrow) binding events within the axoplasm. Squid giant axon axoplasm samples were used to image WT, Y18A, and Y18E 3RS-Tau interactions (500 pM Alexa 488-labeled Tau, green) with axonal microtubules (200 nM Alexa 568-labeled Tau, red). Tau binds both statically and dynamically under physiological conditions.

conditions. TIRF microscopy was used to visualize Tau behavior (Figure 6) in ex vivo preparations of axoplasm extruded from the giant axons of Atlantic squid (*Loligo pealeii*). The extruded axoplasm samples were perfused with a mixture of Alexa 568-labeled WT, Y18A, or Y18E 3RS-Tau to visualize microtubules and Alexa 488-labeled WT, Y18A, or Y18E 3RS-Tau to observe single-molecule events (Supplemental Movies S4 and S5). Nonphosphorylatable Y18A 3RS-Tau had a static population of $82.0 \pm 3.8\%$ (Figure 7 and Supplemental Table S3). This was statistically significant from static populations for WT ($74.0 \pm 4.4\%$) and Y18E 3RS-Tau ($73.2 \pm 4.4\%$; $p < 0.05$; Figure 7 and Supplemental Table S3). These results highlight the importance of using an unphosphorylatable construct to prevent possible ex vivo phosphorylation at Y18. On the basis of these data, we conclude that the Y18E-mediated shift toward the dynamic state observed in vitro is maintained within the axoplasm. Unlike the in vitro dwell times, all ex vivo dwell times for WT, Y18A, and Y18E 3RS-Tau best fit a single exponential function. There was no difference in the ex vivo static dwell times (Supplemental Figure S6, A–F, and

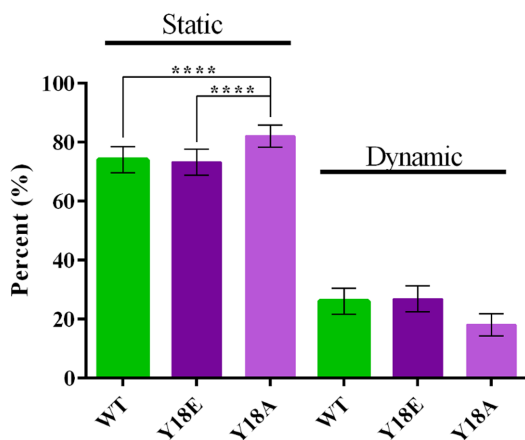


FIGURE 7: Tau's binding equilibrium between static and dynamic states is maintained ex vivo. Bar graph comparing the percentage (\pm SD) of static to dynamic events for Y18E and Y18A 3RS-Tau in the axoplasm preparation. As observed in vitro (Figures 3 and 5), a shift in Tau's equilibrium toward the dynamic state was observed upon introduction of negative charge at Y18. **** $p < 0.05$. Events: Y18A, 972 ($N = 5$); WT, 1129 ($N = 4$); and Y18E, 757 ($N = 5$).

Supplemental Table S3) for WT, Y18A, and Y18E 3RS-Tau. We observed ex vivo dwell times that were an order of magnitude shorter than the in vitro dwell times (Supplemental Figures S2, S4, and S5). This difference was previously observed (Janning et al., 2014) and can most likely be attributed to the increased ionic strength found under physiological conditions. This is the first evidence that the static–dynamic equilibrium of Tau on the microtubule surface observed in vitro is present under conditions within the axon.

DISCUSSION

Recently we showed that Tau's ability to inhibit kinesin-1 motility differs with isoform (McVicker et al., 2014). However, the cellular means of regulating Tau's inhibition of kinesin-1 is still not understood. Y18 phosphorylation is of particular interest because of its role in preventing the inhibition of axonal transport in the disease state (Kanaan et al., 2012) and its possible involvement in stabilizing a nondisease-state dynamic folded conformation of Tau in solution (Jeganathan et al., 2006). Our results (Figure 2) are the first evidence of phosphorylation regulating Tau's ability to inhibit kinesin-1.

We hypothesized two possible explanations for the reduced inhibition of kinesin-1. Introduction of negative charge at Y18 could shift the static–dynamic state equilibrium toward the less inhibitory dynamic state. Alternatively, the negative charge at Y18 could decrease Tau's affinity for the microtubule surface, effectively reducing the number of Tau obstacles for kinesin-1 to circumnavigate. Specifically for our kinesin-1 motility assay conditions (1:5 Tau:tubulin; Figure 2), a final concentration of 200 nM Tau was used, for which WT 3RS-Tau had a fraction bound of 87% (174 nM) compared with Y18E 3RS-Tau's fraction bound of 59% (118 nM; based on binding assay results; Figure 4). However, we also found that Y18E 3RS-Tau's shift toward the dynamic state is maintained at comparable fractions of Tau bound to the microtubule surface (5–9 nM; Figure 5). Therefore the dynamic state shift observed upon Y18 phosphorylation is intrinsic to behavior of individual Tau molecules and is not dependent on the amount of Tau bound to the microtubule.

Nonetheless, the difference in affinity for the microtubule between WT and Y18E 3RS-Tau must still be taken into account. Although the exact structural changes that underlie static versus dynamic binding are not well understood, the negative charge-mediated decrease in affinity indicates that long-range structural interactions may affect protein binding and behavior. Based on the behavior observed in the high-concentration dynamics assays (Figure 3), 134 nM of the bound WT 3RS-Tau would be static, whereas for Y18E, 3RS-Tau 56 nM would be static. For 1 μ M microtubules, statically bound WT 3RS-Tau would occupy 13% of the available kinesin-1-binding sites, whereas static Y18E 3RS-Tau would occupy 5% of the available binding sites. This indicates that Y18E 3RS-Tau's decreased inhibition of kinesin-1 is due to a combination of a decreased bound fraction and an equilibrium shift toward the dynamic state. Ultimately, this leads to a reduction in the number of static Tau obstacles that kinesin-1 encounters on the microtubule surface.

It was previously demonstrated that with increasing concentration, Tau forms multiprotein patches on the microtubule surface (Dixit et al., 2008). Our high-concentration behavioral assays (Figure 3 and Supplemental Table 3) show two populations of WT 3RS-Tau static dwell times. The long dwell time (Supplemental Table 3 and Supplemental Figures S2 and S3) may be indicative of multiprotein complexes formed by N-terminal region-mediated Tau-Tau interactions (Feinstein et al., 2016). The loss of a short static dwell time for Y18E 3RS-Tau (Supplemental Table S3 and Supplemental Figure S2) indicates that with the introduction of negative charge at high concentration, static binding may only occur when multiprotein complexes are

formed. In addition, the introduction of N-terminal negative charge may disrupt complex formation (Feinstein *et al.*, 2016), which would lead to the observed shift toward dynamic binding at high concentration (Supplemental Table S3). In keeping with these results, we previously showed that 4RL-Tau, which has two acidic N-terminal inserts, forms smaller multiprotein complexes and is shifted more toward dynamic binding than 3RS-Tau, which has no acidic inserts (McVicker *et al.*, 2014). At low concentration (Figure 3), static binding is not governed by concentration-driven complex formation.

Tau's inhibition of kinesin-1 motility does not affect velocity (Supplemental Table S2; Dixit *et al.*, 2008). We previously demonstrated that whereas kinesin-1 pauses both in the presence and absence of Tau, the pause-step frequency does not change (Hoeprich *et al.*, 2014). Therefore the effect of pausing on velocity is not significant. An increase in run termination would lead to the observed decrease in run length.

We previously reported the importance of the lattice structure in regulation of Tau isoforms' static–dynamic state equilibria (McVicker *et al.*, 2014). Tau's ability to inhibit kinesin-1 motility is also regulated by lattice structure (McVicker *et al.*, 2011). On guanosine-5'-(α,β -methylene)triphosphate-stabilized microtubules, 3RS-Tau binds dynamically and does not inhibit kinesin-1 motility (McVicker *et al.*, 2011, 2014). Tau's inhibitory effect is restored on paclitaxel-stabilized microtubules, where 3RS-Tau's binding equilibrium is shifted toward the static state (McVicker *et al.*, 2011, 2014). The present study demonstrates that lattice regulation is not the only means available for control of Tau's binding equilibrium. Controlling Tau's intrinsic equilibrium through phosphorylation and the microtubule lattice structure through nucleotide binding states and PTMs (McVicker *et al.*, 2014; Yu *et al.*, 2015) gives the cell greater flexibility in regulating Tau obstacles and allows for continued AT. We demonstrated that Tau's static–dynamic state equilibrium is maintained under physiological conditions and that the shift toward the dynamic state that we observed in vitro occurs ex vivo (Figure 5). As we showed and as has been previously reported (Janning *et al.*, 2014), Tau binds both dynamically and transiently to the microtubule surface under physiological conditions. Extending this observation, we emphasize the importance of regulating these dynamic interactions to control Tau function. Note that the dwell times reported here are longer than those previously reported (Janning *et al.*, 2014), which may relate to the different Tau constructs and neuronal systems used and highlight the importance of further study to better understand Tau dynamics in vivo.

Within the axon phosphorylation of Y18, the last residue of the PAD not only shields the PAD (Kanaan *et al.*, 2012), but, as our results show, the negative charge provided by phosphorylation facilitates a dynamic state shift independent of fraction bound (Figures 3 and 5). This gives the cell two levels of regulating Tau's function by preventing Tau signaling through the PAD and Tau's physical inhibition of kinesin-1 motility. In this model, while Y18 is phosphorylated, individual motors continue to transport cargo (Figure 8). Dephosphorylation of Y18 leads to signaling activation (Kanaan *et al.*, 2012) and increased physical inhibition of kinesin-1 motility (Figure 8). Exposure of Tau's PAD has been shown to ultimately activate glycogen synthase kinase 3 β (GSK-3 β), which in addition to phosphorylating Tau (Lovestone *et al.*, 1996; Martin *et al.*, 2013), can phosphorylate kinesin light chains (Morfini *et al.*, 2002) (Figure 8). This leads to further disruption of cargo–motor interactions, leading to dissociation of motors from cargo, thereby allowing cargo delivery (Morfini *et al.*, 2002; Figure 8).

PAD shielding by phosphorylation of Y18 (Kanaan *et al.*, 2012) may partly depend on structural change. The misregulation of Tau's

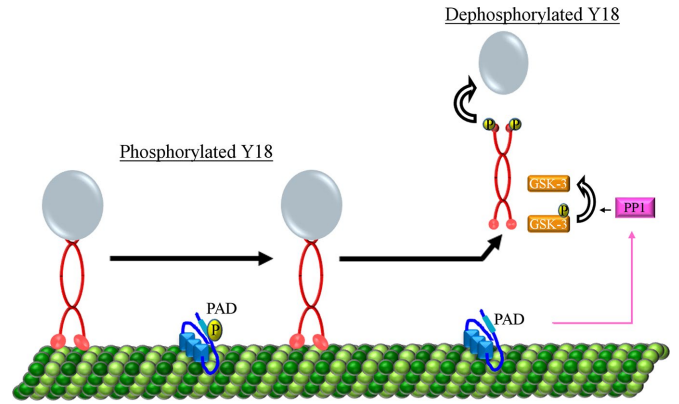


FIGURE 8: Model of Tau regulation. Results from the present work indicate that Y18 phosphorylation (yellow) not only prevents PP1 activation induced by exposed PAD (light blue; Kanaan *et al.*, 2012), but it also stabilizes Tau (blue) in the dynamic state, allowing for continued kinesin-1 (red) mediated cargo transport. On the other hand, Y18 dephosphorylation would shift Tau's equilibrium toward the more inhibitory static state while allowing PAD activation of PP1 (pink) upon exposure. PP1 would then dephosphorylate and activate GSK-3 β (orange), which in turn phosphorylates kinesin-1 light chains and promotes dissociation from its transported cargoes. Thus misregulation of Tau's dynamic equilibrium could promote neuronal degeneration by compromising localized delivery of kinesin-1 cargoes.

structure (Elbaum-Garfinkle and Rhoades, 2012) and therefore its function could be a common pathway by which neurodegeneration occurs in diseases in which shifts in isoform expression and aberrant phosphorylation lead to the same outcome (Qian *et al.*, 2013; Gerson *et al.*, 2014).

Control of Tau's function is further complicated by abnormal modifications that occur in the disease state (Morris *et al.*, 2015). Our group and others previously showed that Tau's ability to inhibit kinesin-1 motility differs with isoform (Vershinin *et al.*, 2007; Dixit *et al.*, 2008; McVicker *et al.*, 2011), as does the static–dynamic state equilibrium (McVicker *et al.*, 2014). The results we present here indicate that phosphorylation provides a common means of regulating the isoforms and their equilibria. Perturbing the equilibrium between the static and dynamic states would lead to disruption of cargo transport within the axon by disrupting inhibition of kinesin-1 motility and release of cargo. Given our results, it is highly likely that the equilibrium between the static and dynamic states is spatially regulated in order to effectively control local cargo delivery. This localized signaling would require the involvement of multiple signaling pathways and a complex pattern of Tau phosphorylation. It is not known how these phosphorylation events affect the normal behavior of the protein or how the cell balances N- and C-terminal phosphorylation to maintain a working static–dynamic state equilibrium. In addition to phosphorylation, Tau is subject to acetylation (Kamah *et al.*, 2014) and methylation (Funk *et al.*, 2014), whose purposes in the regulation of Tau's function have yet to be fully understood. It is imperative that the balance of nondisease state modifications, especially phosphorylation, is understood, given that one of the first steps in neurodegeneration may be disruption of these normal modifications. We have begun to elucidate the importance of regulating phosphorylation at specific sites to control Tau function. Here, we highlighted new implications for the cellular control of Tau's static–dynamic state equilibrium in axonal transport under both normal and disease-state conditions.

MATERIALS AND METHODS

All protein work and experiments were done in Brinkley's Reassembly Buffer 80 (BRB80; 80 mM 1,4-piperazinediethanesulfonic acid [PIPES], 1 mM ethylene glycol tetraacetic acid [EGTA], 1 mM MgCl₂, pH 6.9, at room temperature) unless otherwise noted.

Tau construct generation, purification, and labeling

Alanine/glutamic acid 3RS-Tau constructs were generated using the QuikChange II XL Site-Directed Mutagenesis Kit (Agilent Technologies, Santa Clara, CA). Constructs were then expressed in BL21-CodonPlus(DE3)-RP *Escherichia coli* cells (Stratagene, La Jolla, CA) and purified using Q and SP Sepharose (Sigma-Aldrich, St. Louis, MO) affinity column chromatography (McVicker *et al.*, 2011, 2014). After purification, samples were dialyzed against BRB80, and protein concentrations were determined with the bicinchonic acid (BCA) assay (Pierce, Rockford, IL) using WT 3RS-Tau standards. The concentrations were then validated with SDS-PAGE gels (Bio-Rad, Hercules, CA). For labeling, samples were incubated with 10-fold molar excess of dithiothreitol (DTT) at room temperature for 2 h, followed by DTT removal with a 2 ml of 7K MWCO Zeba spin desalting column (Pierce, Rockford, IL). Samples were then incubated with threefold molar excess of Alexa Fluor (488, 532, or 568) C5 Maleimide (Invitrogen Molecular Probes, Carlsbad, CA) for 2 h at room temperature. Excess fluor was removed with desalting columns. A 640 Spectrophotometer (Beckman, Pasadena, CA) was used to determine the labeling efficiency using the following Alexa extinction coefficients: Alexa 488, 71,000 cm⁻¹ M⁻¹ at 495 nm; Alexa 532, 78,000 cm⁻¹ M⁻¹ at 532 nm; and Alexa 568, 88,000 cm⁻¹ M⁻¹ at 578 nm. The protein concentration was determined using the BCA assay, and the ratio of fluor concentration to protein concentration was calculated. All Tau proteins had labeling efficiencies of 30–86% (detailed in Supplemental Table S1).

Tubulin purification and microtubule preparation

Tubulin was purified from bovine brain obtained from Vermont Livestock Slaughter & Processing (Ferrisburgh, VT) as previously described (McVicker *et al.*, 2014). Purified tubulin was clarified by ultracentrifugation (20 min, 95,000 rpm, 4°C) in an Optima TLX Ultracentrifuge (Beckman, Pasadena, CA). After clarification, tubulin was mixed with rhodamine-labeled tubulin (Cytoskeleton, Denver, CO) at a 1:200 (labeled:unlabeled) ratio and supplemented with 1 mM GTP (Sigma-Aldrich). This mixture was incubated for 20 min at 37°C. After polymerization, microtubules were stabilized with 20 μM paclitaxel (Sigma-Aldrich). After clarification, tubulin concentration was calculated with the spectrophotometer using the tubulin extinction coefficient of 115,000 cm⁻¹ M⁻¹ at 280 nm.

Coverslip preparation and flow chamber assembly

For silanization, glass coverslips were incubated in 100% methanol for 2 h with shaking. Methanol-washed coverslips were then plasma cleaned (Harrick Plasma Cleaner; Harrick Plasma, Ithaca, NY) for 2–5 min and incubated in a silane mixture (97% toluene [Sigma-Aldrich], 2% 2-methoxy(polyethyleneoxy)propyltrimethoxysilane [Gelest, Morrisville, PA], and 1% butylamine [Acros Organics, Morris Plains, NJ]) with flowing nitrogen gas for 90 min (Lowndes and Nelson, 2013). Coverslips were washed in toluene (Lowndes and Nelson, 2013) and then dried and cured with flowing nitrogen gas for 30 min. Norland optical adhesive (Norland Products, Cranbury, NJ) was used to construct flow chambers by adhering ARTUS shims (ARTUS, Eaglewood, NJ) to silanized glass coverslips before 15 min of UV irradiation (McVicker *et al.*, 2011).

In vitro TIRF dynamics assay

Paclitaxel-stabilized microtubules were incubated with WT, alanine (Y18A), single-glutamic acid (Y18E), or double-glutamic acid (dE) 3RS-Tau constructs at a 1:3000 Tau:tubulin ratio (10–12 nM) 30 min before imaging. For imaging, washes and incubations were performed with BRB80+OS (BRB80 supplemented with a previously published oxygen scavenging system; McVicker *et al.*, 2011). Flow chambers were incubated with monoclonal anti-β III (neuronal) tubulin antibodies (Sigma-Aldrich) at 33 μg/ml for 5 min, followed by a 5-min 2× chamber volume wash with 2 mg/ml bovine serum albumin (BSA; Sigma-Aldrich). Alternatively, a 5-min 2.5% Pluronic F-127 (Sigma-Aldrich) incubation was done before the chambers were washed (10× chamber volume) with BSA for 5 min to remove excess Pluronic F-127. The chambers were then incubated for 12 min with microtubule/Tau mixtures diluted to 0.5–1 μM. Finally, the chambers were washed with 160–333 pM Tau (1:3000 imaging concentration) for 2–4 min to remove nonadherent microtubules. All Tau and microtubule dilutions were made in warm (37°C) BRB80+OS.

To observe Tau's behavior at a 1:5 Tau:tubulin ratio, the needed concentration of unlabeled WT or Y18E 3RS-Tau (200 nM) was spiked with 500 pM Alexa 488-labeled WT or Y18E 3RS-Tau. Microtubules were stabilized as described and incubated with either the WT or Y18E 3RS-Tau spike mixture 30 min before imaging. As before, washes and incubations were performed with warm BRB80+OS. Microtubule/Tau mixtures were diluted to a final imaging concentration of 1 μM. The chambers were prepared as previously detailed and then incubated with diluted microtubule/Tau mixtures. The chambers were washed with warm WT or Y18E 3RS-Tau mixtures (concentrations given earlier) to remove nonadherent microtubules and keep Tau concentrations constant (2–4 min).

An inverted Eclipse Ti-U Microscope (Nikon, Melville, NY) with a 100× PlanApo objective lens (1.49 numerical aperture [NA]) and auxiliary 1.5× magnification and an XR/Turbo-Z (Stanford Photonics, Palo Alto, CA) camera running Piper Control version 2.3.39 or 2.6.09 (Stanford Photonics) was used to perform TIRF microscopy as previously described (Previs *et al.*, 2012, 2015; Hoepflich *et al.*, 2014). Alexa 488-labeled Tau and rhodamine-labeled tubulin were excited and imaged as previously described with 473- or 532 nm-argon lasers and previously reported emission filters (McVicker *et al.*, 2014). Images were collected at room temperature at 10 frames/s, 95 or 93 nm/pixel, 50 frames for microtubules, and 500 or 1000 frames for Tau.

TIRF binding assay

The affinity and cooperativity of 3RS-Tau binding to microtubules were assessed using a TIRF-based binding assay. Microtubules were prepared as described except that labeling was carried out with porcine HiLyte 488-labeled tubulin (Cytoskeleton) at a 1:400 labeled:unlabeled ratio. Tau constructs were labeled with Alexa 532 as described. As with the in vitro dynamics assay, all dilutions, washes, and incubations were done in BRB80+OS. Final Tau and microtubule dilutions were done in warm BRB80+OS as described. Microtubules were polymerized as described except that no Tau was added before imaging. Microtubules were then flowed into prepared flow chambers at 1.5 μM as described. Initially, chambers were washed to remove nonadherent microtubules. Then 50 nM Tau was flowed in and imaged. After this, increasing concentrations of Tau were flowed in and imaged until a final concentration of 650 nM was reached. Twenty frames of Tau were collected at 10 frames/s for each concentration. Imaging was done on the same system with the same conditions used for the in vitro TIRF dynamics assay.

Ex vivo TIRF dynamics assay

To visualize Tau under physiological conditions, Atlantic squid (*L. pealeii*; Marine Biological Laboratory, Woods Hole, MA) axons were isolated and their axoplasms extruded following previously established protocols (Brady *et al.*, 1993; Song and Brady, 2013). Briefly, flow chambers were constructed using $25 \times 75 \times \sim 1$ mm glass slides (VWR Scientific, Radnor, PA) and strips of 22×22 mm coverslips (VWR Scientific) cut with a diamond-tipped pen and coated with Compound III Silicon grease (Dow Corning, Midland, MI). Paired axoplasms were extruded onto individual chamber slides. Flow chambers were then completed by adding a top coverslip that was silanized as previously described. Chambers were then secured with a 1:1:1 lanoline, Vaseline, and paraffin mixture (Song and Brady, 2013).

Tau constructs were initially diluted in 20 mM 4-(2-hydroxyethyl)-1-piperazineethanesulfonic acid (HEPES; pH 7.2), and all axoplasm imaging was done in Buffer X/0.8 (437.5 mM potassium aspartate, 162.5 mM taurine, 87.5 mM betaine, 62.5 mM glycine, 25 mM HEPES, 16.25 mM $MgCl_2$, 12.5 mM EGTA, 3.75 mM $CaCl_2$, 1.25 mM glucose, pH 7; Song and Brady, 2013) diluted to Buffer X/2 with double-distilled H_2O . Perfusion mixtures were made with 200 nM Alexa 568-labeled Y18A or Y18E 3RS-Tau, 500 pM Alexa 488-labeled Y18A or Y18E 3RS-Tau, and a final ATP concentration of 1 mM. After perfusion, axoplasms were incubated at room temperature for 20 min before imaging began. An inverted Eclipse Ti microscope (Nikon) with a 100 \times Apochromatic objective lens (1.49 NA) was used to carry out TIRF microscopy with 488-nm (LU-NV laser combiner; Nikon) and 561-nm (MLC400 Monolithic Laser Combiner; Agilent) lasers and emission band-pass filter sets 525/50 nm and 600/50 nm (Chroma Technology, Bellows Falls, VT). An iXon Ultra 897 camera (BT12 7AL; Andor, Belfast, United Kingdom) running NIS-Elements AR version 4.30.02 (Nikon) was used to image Tau in the axoplasm. The relatively high concentration of Alexa 568 (200 nM)-labeled Tau allowed for visualization of microtubules, whereas the low Alexa 488 (500 pM)-labeled Tau concentration allowed imaging of single Tau molecules. We collected 100 frames each at room temperature of microtubules and Tau with an interval of 0.3 s and a pixel size of $0.16 \times 0.16 \mu m$.

In vitro kinesin-1 motility assay

Motility assays were performed with a truncated (560 amino acids) *Drosophila melanogaster* biotin-tagged kinesin-1 construct (gift from Hancock lab, Pennsylvania State University). Motors were labeled with streptavidin-conjugated Qdot 655 (Life Technologies, Carlsbad, CA) at a 1:4 motor:Qdot ratio. Paclitaxel-stabilized microtubules were prepared as described except that after polymerization, microtubules were centrifuged at room temperature for 30 min before the pellet was resuspended in motility assay buffer (MAB; 10 mM PIPES, pH 7.4, at room temperature, 50 mM potassium acetate, 4 mM magnesium acetate, 1 mM EGTA) at 37°C supplemented with an oxygen scavenging system (MAB+OS) as previously described (Hoeprich *et al.*, 2014). Before imaging, microtubules were incubated with Tau (Alexa 488 labeled or unlabeled WT or Y18E 3RS-Tau) at a 1:5 Tau:tubulin ratio for 20 min at 37°C. Flow chambers were prepared by incubation with monoclonal anti-tubulin antibodies (as already described) diluted with MAB+OS. Blocking and washing were done as previously detailed. Briefly, chambers were blocked with 0.5 mg/ml BSA in MAB+OS before 1 μM of microtubules or microtubules/Tau were added and incubated as for the Tau behavioral assays. Nonadherent microtubules were removed with an MAB+OS wash supplemented with paclitaxel. A working concentration of 20–50 pM kinesin-1 along with 1 mM ATP was added just before imaging. Imaging was performed on the same system as the in vitro Tau assays. Qdots were excited with the 473-nm laser, and all movies were acquired at 5 frames/s.

Data analysis

In vitro TIRF dynamics assays. ImageJ version 1.48 (National Institutes of Health, Bethesda, MD) was used to create kymographs of Tau interacting with the microtubule using the MultipleKymograph plug-in. To determine dwell times, the MTrackJ plug-in was used to measure the length of events that were clearly static or dynamic. Eleven percent of events display switching and were not included in further analysis. Only events that began, remained, and ended on the microtubule during the imaging period were used. Dynamic and static dwell times were exported to GraphPad Prism version 6.00 (GraphPad Software, La Jolla, CA). Cumulative frequency distribution plots were generated for each population and fit to one- or two-phase exponential functions. Average dwell times were calculated as the time constant of the exponential function. The goodness of the fit (R^2) and the 95% confidence bands are also reported. Fisher's exact test was used to determine statistical significance for static versus dynamic populations of 3RS-Tau construct data sets. All data sets are composites of data collected on different days. High concentration (spike): WT, $N = 8$; Y18E, $N = 8$. Comparable bound fraction: WT, $N = 12$; Y18A, $N = 5$; Y18E, $N = 4$; dE, $N = 5$.

Ex vivo TIRF dynamics assay. Events were tracked using the MTrackJ plug-in for ImageJ. Events were chosen if they lasted more than one frame and if the signal remained within a snap range of 13×13 pixels from one frame to the next (snap range chosen based on maximum diffusive range of a Tau protein; Konzack *et al.*, 2007). Tracks were exported to Excel, and events with a maximum distance from start of $\leq 0.5 \mu m$ were designated static, whereas events $> 0.5 \mu m$ were designated dynamic. GraphPad Prism was used as described to plot the cumulative frequency distribution of the dwell times, to which one-phase exponential functions were fit. The average dwell time was determined from the fit of the exponential function. As before, R^2 and the 95% confidence bands are reported. Statistical significance was determined using chi square with Yates' correction. All data sets comprise data collected on different days (WT, $N = 4$; Y18A, $N = 5$; Y18E, $N = 5$).

TIRF binding assay. The average intensity (Avg I ; arbitrary units) per unit length of Tau binding the microtubule was measured for each frame using the Multi Measure plug-in for ImageJ. In GraphPad Prism, Avg I per unit length was plotted versus [Tau]. Binding curves were fitted to one-site-specific binding with Hill slope, which was used to determine the Hill coefficient and K_D using the Hill equation:

$$\frac{\text{Avg } I}{\text{Unit length}} = \frac{A_{\max} [\text{Tau}]^h}{K_D^h + [\text{Tau}]^h}$$

where h is the Hill coefficient and A_{\max} is the maximum Avg I per unit length. The Avg I per unit length reported here was normalized to A_{\max} . Tau's fraction bound, f_B , for the kinesin-1 motility assay was determined using the equation

$$f_B = \frac{[\text{MT}]}{K_{D_{\text{Tau}}} + [\text{MT}]}$$

where [MT] is the concentration of microtubules used for imaging and $K_{D_{\text{Tau}}}$ is the affinity of Tau for the microtubule surface calculated in the binding assay. All data sets comprise data collected on different days (WT, $N = 4$; Y18A, $N = 3$; Y18E, $N = 3$).

In vitro kinesin-1 motility assay. Data were analyzed as reported previously (Hoeprich *et al.*, 2014). Briefly, the MTrackJ plug-in for

ImageJ was used to measure motility, and the segmented line tool was used to measure track lengths. Average velocity was plotted as a histogram and fitted to a Gaussian distribution. The mean and SD are reported here. Previously outlined methods (Thompson *et al.*, 2013) were used to generate cumulative frequency plots for run lengths corrected for microtubule track length effects (by resampling the data) and reported here (99% confidence level of data resampling repeated 10,000 times). Statistical significance was determined as previously described (Thompson *et al.*, 2013). All data sets comprise data collected on different days (no Tau, $N = 10$; WT, $N = 10$; Y18E, $N = 10$).

ACKNOWLEDGMENTS

We thank David Warshaw and Guy Kennedy for training, use, and technical support with the TIRF microscope at the University of Vermont. We give special thanks to Vermont Livestock Slaughter & Processing (Ferrisburgh, VT) for continued support of our work. We also thank the Marine Biological Laboratory for providing an extraordinary working environment. We thank Lynne Chang (Nikon, Melville, NY) for provision of and technical support for the TIRF microscope used at the Marine Biological Laboratory, William Hancock for use of his kinesin-1 construct, and Scott Brady, Jason Stumpff, Lynn Chrin, Phillipe Mouchati, Rehan Ali, Minsu Kang, and Henry Thomsett for support at different stages in the development of this work. This work was supported by National Institute of General Medical Sciences/National Institutes of Health funding to C.B. (GM101066) and G.M. (NS066942A).

REFERENCES

- Andreadis A (2005). Tau gene alternative splicing: expression patterns, regulation and modulation of function in normal brain and neurodegenerative diseases. *Biochim Biophys Acta* 1739, 91–103.
- Ballatore C, Lee VM, Trojanowski JQ (2007). Tau-mediated neurodegeneration in Alzheimer's disease and related disorders. *Nat Rev Neurosci* 8, 663–672.
- Brady ST, Richards BW, Leopold PL (1993). Assay of vesicle motility in squid axoplasm. *Methods Cell Biol* 39, 191–202.
- Dixit R, Ross JL, Goldman YE, Holzbaur EL (2008). Differential regulation of dynein and kinesin motor proteins by tau. *Science* 319, 1086–1089.
- Elbaum-Garfinkle S, Rhoades E (2012). Identification of an aggregation-prone structure of tau. *J Am Chem Soc* 134, 16607–16613.
- Feinstein HE, Benbow SJ, LaPointe NE, Patel N, Ramachandran S, Do TD, Gaylord MR, Huskey NE, Dressler N, Korff M, *et al.* (2016). Oligomerization of the microtubule associated protein tau is mediated by its N-terminal sequences: implications for normal and pathological tau action. *J Neurochem* 137, 939–954.
- Funk KE, Thomas SN, Schafer KN, Cooper GL, Liao Z, Clark DJ, Yang AJ, Kuret J (2014). Lysine methylation is an endogenous post-translational modification of tau protein in human brain and a modulator of aggregation propensity. *Biochem J* 462, 77–88.
- Gerson JE, Sengupta U, Lasagna-Reeves CA, Guerrero-Munoz MJ, Troncoso J, Kaye D (2014). Characterization of tau oligomeric seeds in progressive supranuclear palsy. *Acta Neuropathol Commun* 2, 73.
- Goode BL, Chau M, Denis PE, Feinstein SC (2000). Structural and functional differences between 3-repeat and 4-repeat tau isoforms. Implications for normal tau function and the onset of neurodegenerative disease. *J Biol Chem* 275, 38182–38189.
- Hinrichs MH, Jalal A, Brenner B, Mandelkow E, Kumar S, Scholz T (2012). Tau protein diffuses along the microtubule lattice. *J Biol Chem* 287, 38559–38568.
- Hoepflich GJ, Thompson AR, McVicker DP, Hancock WO, Berger CL (2014). Kinesin's neck-linker determines its ability to navigate obstacles on the microtubule surface. *Biophys J* 106, 1691–1700.
- Janning D, Igaev M, Sundermann F, Bruhmann J, Beutel O, Heinisch JJ, Bakota L, Piehler J, Junge W, Brandt R (2014). Single-molecule tracking of tau reveals fast kiss-and-hop interaction with microtubules in living neurons. *Mol Biol Cell* 25, 3541–3551.
- Jeganathan S, von Bergen M, Brutlach H, Steinhoff HJ, Mandelkow E (2006). Global hairpin folding of tau in solution. *Biochemistry* 45, 2283–2293.
- Kamah A, Huvent I, Cantrelle FX, Qi H, Lippens G, Landrieu I, Smet-Nocca C (2014). Nuclear magnetic resonance analysis of the acetylation pattern of the neuronal Tau protein. *Biochemistry* 53, 3020–3032.
- Kanaan NM, Morfini G, Pigino G, LaPointe NE, Andreadis A, Song Y, Leitman E, Binder LI, Brady ST (2012). Phosphorylation in the amino terminus of tau prevents inhibition of anterograde axonal transport. *Neurobiol Aging* 33, 826.e15–30.
- Kanaan NM, Morfini GA, LaPointe NE, Pigino GF, Patterson KR, Song Y, Andreadis A, Fu Y, Brady ST, Binder LI (2011). Pathogenic forms of tau inhibit kinesin-dependent axonal transport through a mechanism involving activation of axonal phosphotransferases. *J Neurosci* 31, 9858–9868.
- Konzack S, Thies E, Marx A, Mandelkow EM, Mandelkow E (2007). Swimming against the tide: mobility of the microtubule-associated protein tau in neurons. *J Neurosci* 27, 9916–9927.
- LaPointe NE, Morfini G, Gaisina IN, Kozikowski AP, Binder LI, Brady ST (2009). The amino terminus of tau inhibits kinesin-dependent axonal transport: implications for filament toxicity. *J Neurosci Res* 87, 440–451.
- Larson M, Sherman MA, Amar F, Nuvoletone M, Schneider JA, Bennett DA, Aguzzi A, Lesne SE (2012). The complex PrP(c)-Fyn couples human oligomeric Abeta with pathological tau changes in Alzheimer's disease. *J Neurosci* 32, 16857–16871a.
- Lee G, Newman ST, Gard DL, Band H, Panchamoorthy G (1998). Tau interacts with src-family non-receptor tyrosine kinases. *J Cell Sci* 111, 3167–3177.
- Lovestone S, Hartley CL, Pearce J, Anderton BH (1996). Phosphorylation of tau by glycogen synthase kinase-3 beta in intact mammalian cells: the effects on the organization and stability of microtubules. *Neuroscience* 73, 1145–1157.
- Lowndes M, Nelson WJ (2013). Fabricating surfaces with distinct geometries and different combinations of cell adhesion proteins. *Methods Mol Biol* 1046, 219–230.
- Maday S, Twelvetrees AE, Moughamian AJ, Holzbaur EL (2014). Axonal transport: cargo-specific mechanisms of motility and regulation. *Neuron* 84, 292–309.
- Martin L, Latypova X, Wilson CM, Magnaudeix A, Perrin M-L, Yardin C, Terro F (2013). Tau protein kinases: involvement in Alzheimer's disease. *Ageing Res Rev* 12, 289–309.
- McVicker DP, Chrin LR, Berger CL (2011). The nucleotide-binding state of microtubules modulates kinesin processivity and the ability of Tau to inhibit kinesin-mediated transport. *J Biol Chem* 286, 42873–42880.
- McVicker DP, Hoepflich GJ, Thompson AR, Berger CL (2014). Tau interconverts between diffusive and stable populations on the microtubule surface in an isoform and lattice specific manner. *Cytoskeleton (Hoboken)* 71, 184–194.
- Morfini G, Szebenyi G, Elluru R, Ratner N, Brady ST (2002). Glycogen synthase kinase 3 phosphorylates kinesin light chains and negatively regulates kinesin-based motility. *EMBO J* 21, 281–293.
- Morris M, Knudsen GM, Maeda S, Trinidad JC, Ioanoviciu A, Burlingame AL, Mucke L (2015). Tau post-translational modifications in wild-type and human amyloid precursor protein transgenic mice. *Nat Neurosci* 18, 1183–1189.
- Panda D, Samuel JC, Massie M, Feinstein SC, Wilson L (2003). Differential regulation of microtubule dynamics by three- and four-repeat tau: implications for the onset of neurodegenerative disease. *Proc Natl Acad Sci USA* 100, 9548–9553.
- Previs MJ, Beck Previs S, Gulick J, Robbins J, Warshaw DM (2012). Molecular mechanics of cardiac myosin-binding protein C in native thick filaments. *Science* 337, 1215–1218.
- Previs MJ, Prosser BL, Mun JY, Previs SB, Gulick J, Lee K, Robbins J, Craig R, Lederer WJ, Warshaw DM (2015). Myosin-binding protein C corrects an intrinsic inhomogeneity in cardiac excitation-contraction coupling. *Sci Adv* 1, e1400205.
- Qian W, Jin N, Shi J, Yin X, Jin X, Wang S, Cao M, Iqbal K, Gong CX, Liu F (2013). Dual-specificity tyrosine phosphorylation-regulated kinase 1A (Dyrk1A) enhances tau expression. *J Alzheimers Dis* 37, 529–538.
- Song Y, Brady ST (2013). Analysis of microtubules in isolated axoplasm from the squid giant axon. *Methods Cell Biol* 115, 125–137.
- Thompson AR, Hoepflich GJ, Berger CL (2013). Single-molecule motility: statistical analysis and the effects of track length on quantification of processive motion. *Biophys J* 104, 2651–2661.
- Vershinin M, Carter BC, Razafsky DS, King SJ, Gross SP (2007). Multiple-motor based transport and its regulation by Tau. *Proc Natl Acad Sci USA* 104, 87–92.
- Watanabe A, Hasegawa M, Suzuki M, Takio K, Morishima-Kawashima M, Titani K, Arai T, Kosik KS, Ihara Y (1993). In vivo phosphorylation sites in fetal and adult rat tau. *J Biol Chem* 268, 25712–25717.
- Yu I, Garnham CP, Roll-Mecak A (2015). Writing and reading the tubulin code. *J Biol Chem* 290, 17163–17172.